Full length article

Soret effects on the diffusion-chemistry interaction of hydrogen-air edge flames propagating in transverse gradient evolving mixing layers

Tao Chen [a,b], Suyuan Yu [a,b], Yu Cheng Liu [a,b,c,*]

[a] *Center for Combustion Energy, Tsinghua University, Beijing 100084, China*
[b] *Department of Energy and Power Engineering, Tsinghua University, Beijing 100084, China*
[c] *Key Laboratory for Thermal Science and Power Engineering of Ministry of Education, Tsinghua University, Beijing 100084, China*

ARTICLE INFO

ABSTRACT

The effects of Soret diffusion (SD) on the hydrogen-air edge flame propagation and the diffusion-chemistry interaction are investigated through simulation facilitated by the numerical code *MultiDiffFOAM*. The edge flames in this study gradually develop from a flame kernel into a tri-brachial structure in a hydrogen-air mixing layer that temporally evolves due to transverse reactant concentration gradient. We demonstrate that the responses of flame displacement speed S_d to flame curvature K, stretch rate κ and scalar dissipation rate χ are distinctly influenced by SD. For the linear S_d-K and S_d-κ correlations, SD would result in a smaller Markstein length. Moreover, SD is shown to lead to shifting of the S_d-χ curve towards the regime with larger χ. Compared with the weak influences of SD on the tangential diffusion component $S_{d,t}$ and normal diffusion component $S_{d,n}$, the chemical reaction component $S_{d,r}$ is significantly weakened by SD. The important chemical reactions for edge flame propagation are identified based on sensitivity analysis and their rates are found to be smaller when SD is considered. For the local composition at the flame marker, the mass fraction of H_2 is slightly larger and that of H is obviously smaller when SD is considered. The SD flux of H_2 $j_{H_2}^{SD}$ and that of H j_H^{SD} are both coupled with the driving force $\nabla(lnT)$ along the mixture fraction coordinate. However, the $j_{H_2}^{SD}$ is mainly concentrated on the unburnt side while the j_H^{SD} is on the burnt side. The analyses on decomposed fluxes of H_2 and H along the flame normal direction further suggest that SD would enhance the H_2 mass diffusion but weaken the H mass diffusion. Such opposite effects stem from the distribution features that H_2 is mainly on the unburnt side while H on the burnt side.

1. Introduction

Hydrogen is a zero-carbon emission fuel that facilitates a large flame speed and a broad flammability limit and thus has been receiving increasing attention as one promising fuel for power plants and propulsion systems [1–4]. In many energy and propulsion applications [5–8], the hydrogen and oxidizer streams are supplied separately such that these two streams would undergo the so-called "partially premixed combustion" process governed by the aerodynamic process that takes place in the proximity of a mixing layer. As the reliability of such mixing and combustion processes has been highly desirable, the flame stabilization and blowoff [9,10], and the local extinction and re-ignition of turbulent flames [11,12] associated with the edge flame dynamics in practical systems have been extensively investigated.

The first experimental observation of edge flame was conducted by Phillips [13] in a methane-air mixing layer, in which the edge flame was found to display a tri-brachial structure that contains one rich premixed flame branch (RPFB), one lean premixed flame branch (LPFB) and one tailing diffusion flame branch (DFB). Dold [14] adopted the canonical irreversible one-step chemical reaction model with a low heat release assumption and pointed out that the global propagation speed of edge flame U_{edge} is negatively correlated with the fuel mass fraction gradient $|\nabla Y_F|$ and the maximum value of U_{edge} should be bounded by the laminar flame speed S_L. The effects of heat release on the edge flame propagation were further studied [15] with the results showing the necessity of considering heat release for the curved edge flame front and the re-direction effect. The re-direction effect induced by thermal expansion could lead to the local flow deceleration at the upstream of flame front, which therefore can allow the edge flame to propagate under a speed larger than S_L [16]. Moreover, the maximum value of U_{edge} can be approximated in the limit of infinitely small $|\nabla Y_F|$ as $U_{edge}^{max}/S_L = \sqrt{\rho_u/\rho_b}$, where ρ_u and ρ_b are the unburnt and burnt gas density respectively. Based on the parabolic flame front assumption, it

---

was found that the U_{edge} is negatively correlated with the $|\nabla Y_F|$ [17]. Such correlation has been experimentally validated [18]. While it is obvious that the flame curvature increases with increasing $|\nabla Y_F|$ due to the narrower spatial distribution of flammable mixture, the U_{edge} is thus also found to be negatively correlated with the flame curvature. Chung [19] pointed out that the tri-brachial flame structure would transform into the bi-brachial structure with increasing $|\nabla Y_F|$. Such structure may promote the reduction of U_{edge}. The further increase of $|\nabla Y_F|$ may accommodate a mono-brachial flame with a smaller U_{edge} that could potentially lead to the flame extinction.

The effects of flame stretch on the edge flame propagation were investigated [20] with the results showing that the flame stretch induced by flame curvature can dominate over the flow strain term under large $|\nabla Y_F|$ conditions. Moreover, the U_{edge} shows negative dependence on stretch rate. Buckmaster [11,21] further indicated that the U_{edge} might be positive, zero or negative depending on the stretch rate. A retreating edge flame (with a negative U_{edge}) with a mono-brachial diffusion flame structure can appear when the stretch rate is sufficiently large. After experimental observations of "flame island" in turbulent jet flames [22–25], Buckmaster and Weber [11,26] proposed a theory in which edge flames, being the microstructures of turbulent flames, can play important roles in the local flame extinction and re-ignition, and turbulent flame stabilization. The responses of displacement speed S_d of such microstructures in turbulent flames to local flame curvature and stretch rate were statistically analyzed [12,27,28] using direct numerical simulation data, whose results concluded the negative dependence of S_d on curvature and stretch rate.

Except for the above hydrodynamic characteristics of edge flames in general, intrinsic to the hydrogen-air edge flames also is the Lewis number effect stemming from mass diffusion of different species. Using various species-based Lewis numbers, Im and Chen [29] studied the evolution of edge flame and species mass diffusion in a hydrogen-air mixing layer. The results showed that the hydrogen-air edge flame exhibits a typical tri-brachial structure and the position of maximum heat release rate (HRR) is located adjacent to the stoichiometric line. In addition, the enhancement of propagation speed U_{edge} is mainly caused by the re-direction effect. The various species-based Lewis numbers are also adopted in the investigation [30] about the interaction between a hydrogen-air edge flame and a flow vortex pair, whose results showed that the strong flow strain may lead to the negative stretch rate and S_d. By modeling species diffusion based on binary Fick diffusion (FD), Owston et al. [31–33] systematically studied the effects of ignition, mixture stratification, pressure, ambient temperature and water vapor concentration on the hydrogen-air edge flame dynamics. The results showed that the initial ignition stage has negligible influence on the steady flame propagation. The mixture stratification significantly influences the overall heat release while its effect on S_d is relatively small. The S_d is enhanced considerably by the ambient temperature but varies minimally under different pressures. The water vapor concentration significantly reduces the maximum HRR without showing noticeable effects on U_{edge}. Based on binary FD, the normalized global flame speed is shown to be close to $\sqrt{\rho_u/\rho_b}$ for hydrogen-air and methane/hydrogen-air edge flames in the coflow configuration [9,34]. This is also consistent with Ruetsch's theory [15].

A comprehensive understanding of the hydrogen-air edge flame dynamics requires the detailed modeling and analysis about the mass diffusion process of different species in the multi-component mixture. For laminar edge flames at low Mach number conditions, the mass diffusion of species can be driven by the mass fraction gradient, i.e. FD, and the temperature gradient, i.e. Soret diffusion (SD) [35,36]. SD could drive the light (or heavy) species towards (or away from) the high temperature region. Compared with traditional hydrocarbon fuels, the hydrogen-air edge flames usually facilitate much higher concentrations of the lighter species such as H and H_2, so the mass diffusion of these lighter species can exhibit a strong SD process under the large temperature gradient induced by chemical reactions of the hydrogen-air system.

Based on a one-step overall reaction model, it was demonstrated that SD would change the Markstein number of stretched flames and thus could not be ignored when studying the dynamics of wrinkled flame front [37]. The effects of SD on the hydrogen-air Bunsen flame structure were investigated [38], in which SD was found to be crucial for the accurate prediction of species concentration and temperature under both rich and lean conditions. For planar premixed flames, the SD flux of H was found to decrease the flame propagation speed under most equivalence ratio conditions [39]. The roles of SD in outwardly propagating spherical flames were studied [40] and it was found that SD would assist with the reduction of laminar flame speed. Such effect is more obvious under higher initial temperature and pressure conditions. SD was also revealed to promote the instability of hydrogen-air flames under lean conditions so that the flame front can easily evolve into a cellular structure [41]. The SD flux of H_2 was found to play a significant role in the diffusion enhancement of H_2 from the preheat zone to the reaction zone. This process cannot be omitted for the prediction of extinction limit and burning rate of lean premixed hydrogen-air flame especially when the flame is curved or stretched [42]. Yang et al. [43] studied the response of non-premixed hydrogen-air flame to the flow strain rate in a counterflow configuration. The results indicated that the maximum temperature and strain limit for the flame extinction are both larger when SD is taken into account. The SD of H_2 was found to infuse extra H_2 into the reaction zone of non-premixed flame and enhances the overall reactivity [44]. For the hydrogen-air non-premixed flame, the flamelet modeling results showed that the profiles of H_2 and OH is noticeably influenced by SD [45]. Briones et al. [46] studied the effects of SD on the structure of partially premixed hydrogen-air flames using a counterflow flame configuration. The results showed that the position of reaction zone is pushed away from nozzle due to the smaller flame speed caused by SD, and the H mass fraction and HRR are also reduced.

The previous studies demonstrated that the structure and propagation of hydrogen-air flames can be influenced by SD. However, the effects of SD on premixed and non-premixed flames can be quite different as they appear to promote the reactivity of non-premixed flame but diminish it in the premixed flame. The hydrogen-air edge flame can exhibit the structure of non-premixed flame and the propagation feature of premixed flame, the effects of SD on these features are therefore of our interest. The responses of flame displacement speed to flame curvature, stretch rate and scalar dissipation rate under the influences of SD will be analyzed in details. The flame structure and mass diffusion of individual species will also be discussed to gain a more comprehensive understanding about the influences of SD on hydrogen-air edge flames. The rest of this paper is organized as follows: Section 2 describes the numerical method employed in this study, followed by Section 3 for the discussion and Section 4 for the conclusions.

2. Numerical methodology

2.1. Numerical code

The numerical code *MultiDiffFOAM* [16] developed based on the open source software OpenFOAM-6 is adopted for the hydrogen-air edge flame simulation in this study. The numerical solution of full set of governing equations of the laminar reacting flow is implemented by *MultiDiffFOAM* with the capability describing transport processes of momentum, energy and species mass in the multi-component mixture. The newly developed module in *MultiDiffFOAM* could calculate the viscosity, thermal conductivity and mass diffusivity of multi-component mixture through the mixture average method [47,48]. FD and SD of light species are both considered in *MultiDiffFOAM*. The detailed information of *MultiDiffFOAM* code such as governing equations and mixture average method could be found in our previous work [16,49]. This code has been carefully validated based on the premixed flames and coflow flames of hydrogen-air and methane-air mixture.
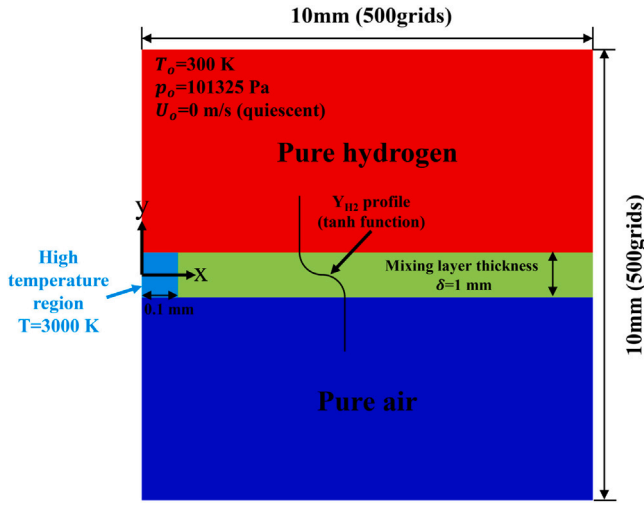
Fig. 1. The schematic of computational domain and initial setup.

2.2. Mass diffusion model

The mass diffusion process of individual species can be driven by the mass fraction gradient, temperature gradient, pressure gradient and body force [48]. For the laminar hydrogen-air edge flames, the mass diffusion due to pressure gradient and body force can be neglected [36,50]. The mass diffusion velocity of ith species $\boldsymbol{U}_i$ thus contains three parts, which can be expressed as follows:

$$\boldsymbol{U}_i = \boldsymbol{U}_i^F + \boldsymbol{U}_i^S + \boldsymbol{U}^C = -\frac{D_i}{Y_i} \cdot \nabla Y_i - \frac{D_i}{X_i}\frac{\Theta_i}{T} \cdot \nabla T + \boldsymbol{U}^C \quad (1)$$

where $\boldsymbol{U}_i^F$, $\boldsymbol{U}_i^S$ and $\boldsymbol{U}^C$ are the Fick diffusion velocity, Soret diffusion velocity and correction diffusion velocity for mass conservation; D_i, X_i and Θ_i are the diffusion coefficient, mole fraction and thermal diffusion ratio of ith species, respectively. D_i and Θ_i are calculated using the TRANSPORT library of CHEMKIN [48] and then are input into *MultiDiffFOAM* code for combustion simulation. SD is considered only for the species whose relative molecular weight is smaller than 5, i.e. H and H_2.

The $\boldsymbol{U}^C$ is derived according to $\sum_{i=1}^{N_s} Y_i \boldsymbol{U}_i = 0$. Moreover, the $\boldsymbol{U}^C$ can be further divided into $\boldsymbol{U}^{C,F}$, the correction caused by FD, and $\boldsymbol{U}^{C,S}$, the correction caused by SD as follows:

$$\boldsymbol{U}^C = \boldsymbol{U}^{C,F} + \boldsymbol{U}^{C,S} = \sum_{i=1}^{N_s} Y_i\left(\frac{D_i}{Y_i} \cdot \nabla Y_i\right) + \sum_{i=1}^{N_s} Y_i\left(\frac{D_i}{X_i}\frac{\Theta_i}{T} \cdot \nabla T\right) \quad (2)$$

Thus, the detailed formula of $\boldsymbol{U}_i$ can be expressed as follows:

$$\begin{aligned}\boldsymbol{U}_i &= \left(\boldsymbol{U}_i^F + \boldsymbol{U}^{C,F}\right) + \left(\boldsymbol{U}_i^S + \boldsymbol{U}^{C,S}\right) \\ &= \left[-\frac{D_i}{Y_i} \cdot \nabla Y_i + \sum_{i=1}^{N_s} Y_i\left(\frac{D_i}{Y_i} \cdot \nabla Y_i\right)\right] \\ &\quad + \left[-\frac{D_i}{X_i}\frac{\Theta_i}{T} \cdot \nabla T + \sum_{i=1}^{N_s} Y_i\left(\frac{D_i}{X_i}\frac{\Theta_i}{T} \cdot \nabla T\right)\right]\end{aligned} \quad (3)$$

In this study, the case only considering the $\boldsymbol{U}_i = \boldsymbol{U}_i^F + \boldsymbol{U}^{C,F}$ of FD is referred to as the **noSoret** case, and the other case considering the full set of Eq. (3) of both FD and SD is referred to as the **Soret** case. By comparing the results of noSoret and Soret cases, the difference between two cases should be due to the SD of H and H_2 and the effects of SD on the edge flame dynamics and the diffusion-chemistry interaction can be analyzed and elucidated.

2.3. Setup of computational domain

The schematic of computational domain and initial setup is shown in Fig. 1. The computation domain contains a pure air region, a pure hydrogen region and a hydrogen-air mixing layer in between. For the initial distribution of reactants mass fraction across the mixing layer (along the y-direction), a hyperbolic tangent profile [31,32,51] is adopted in this study to generate a continuous and steep gradient. The profile of H_2 mass fraction across the mixing layer is given as $Y_{H_2} = \frac{1}{2}\left(1 + tanh\left(\frac{y-y_o}{\delta/4}\right)\right)$, where y_o is the y-coordinate that centers the mixing layer ($y_o = 0$ here). The thickness of initial hydrogen-air mixing layer δ is set as 1 mm. The profiles of O_2 and N_2 mass fraction within the mixing layer can be expressed as $Y_{O_2} = Y_{O_2,air}\left(1 - Y_{H_2}\right)$ and $Y_{N_2} = Y_{N_2,air}\left(1 - Y_{H_2}\right)$, where $Y_{O_2,air}$ (=0.233) and $Y_{N_2,air}$ (=0.767) are the mass fraction of O_2 and N_2 in air. The state of reactants is initially set as $T_o = 300$ K, $p_o = 101325$ Pa, and $U_o = 0$ m/s (quiescent field). The total pressure (101325 Pa) and zero scalar gradient conditions are set for four boundaries. At the beginning of flame simulation, the mixture is ignited by a small high temperature region (3000 K) at the left end of mixing layer (0.1 mm in width along the x-direction). The successful ignition will lead to a hydrogen-air edge flame propagating towards the right along the mixing layer. Such ignition setup was found to have a negligible influence on the steady propagation of edge flame [32]. The total size of computational domain is chosen as 10×10 mm with 500 uniform grid points along each direction as shown in Fig. 1. It is worth noting that the computational setup in Fig. 1 could generate an edge flame whose dynamics parameters such as flame curvature, stretch rate and scalar dissipation rate would be varying during flame propagation due to the evolving gradient of reactant concentration in the mixing layer (especially along the transverse y-direction in Fig. 1). Therefore, the merit of such flame configuration is that it can allow the investigation for the responses of flame displacement speed of edge flame to above parameters with and without considering SD, and the impacts of SD on the edge flame dynamics and the diffusion-chemistry interaction can be elaborated.

A detailed chemical kinetic mechanism containing 10 species and 21 reactions for the hydrogen combustion [52] is utilized. The mesh size of $\Delta L=20$ μm is selected to sufficiently resolve the hydrogen-air edge flame structure based on the mesh independence test as shown in Fig. 2a. The time step 0.1 μs is used to ensure the accuracy and robustness of transient numerical simulation. The implicit Euler scheme, second order upwind scheme and second order center scheme are used for the discretization of transient, convective, and diffusion term, respectively. The pressure-implicit with splitting of operators (PISO) algorithm [53] is used to solve the coupling of velocity and pressure.

In order to study the free propagation process of hydrogen-air edge flame, the domain size should be large enough to eliminate the influence of boundary on edge flames. Owing to these considerations, the domain size independence test is conducted by fixing the domain size along x-direction $L_x = 10$ mm but varying L_y from 10 mm to 22 mm to ensure that $L_y = 10$ mm in our study is large enough to eliminate its influence on flame propagation. Fig. 2b shows the evolution of flame curvature at flame marker (detailed definitions of flame marker and flame curvature are shown in following Section 2.4) with different L_y sizes, in which the difference is quite small. Hence, the legitimacy of using $L_y = 10$ mm for the kind of problem investigated here has been well established.

2.4. Flame marker and parameters of interest

As the major interest of this study is how SD influences the edge flame propagation and the diffusion-chemistry interaction, a common method is to extract information around a flame marker that faithfully traces the leading edge of flame front. Using the same method in previous studies [12,27,28], we determine the position of flame
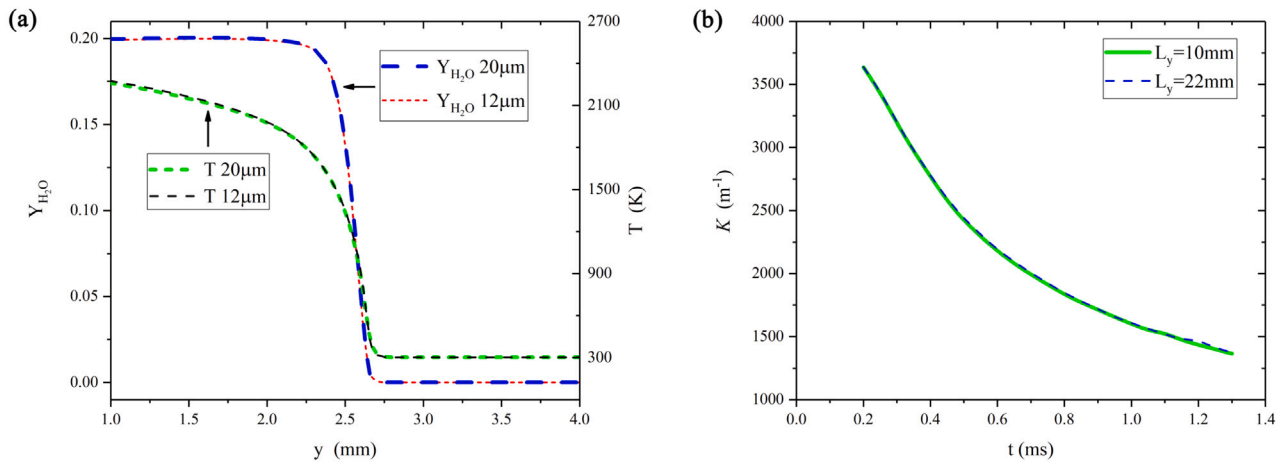
(a)

(b)

Fig. 2. (a) The profiles of temperature and H_2O mass fraction along the stoichiometric line under two mesh size setups. (b) The evolution profiles of flame curvature at flame marker under different L_y size setups (Four L_y size setups are used: 10, 14, 18 and 22 mm and the difference is small. The comparison between 10 and 22 mm is shown here.).
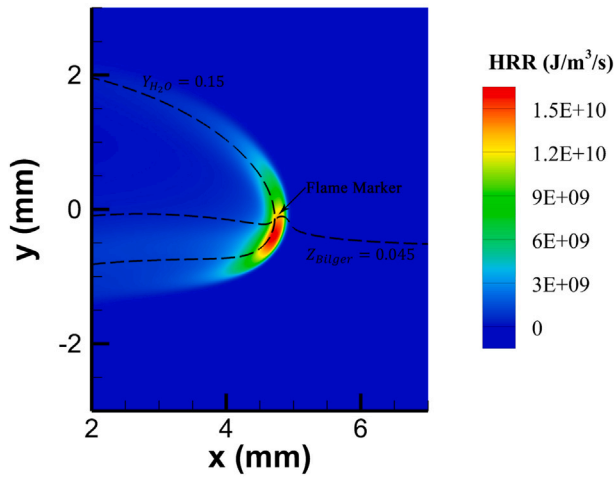

Fig. 3. The schematic of identifying the flame marker through the iso-contours of $Z_{Bilger} = 0.045$ and $Y_{H_2O} = 0.15$.

marker through the intersection of iso-contours of product mass fraction and Bilger mixture fraction. The iso-contour of product mass fraction is usually chosen because it authentically indicates the high HRR region. For the hydrogen-air edge flames in particular, the iso-contour of product mass fraction $Y_{H_2O} = 0.15$ is considered in previous study [31] and is also adopted here. The iso-contour of a particular Bilger mixture fraction that yields the largest laminar flame speed S_L^{max} should be considered to ensure that the flame marker is located at the leading edge [12]. By using the Chemkin PREMIX module [54] with the identical chemical kinetic mechanism, the equivalence ratio of hydrogen-air mixture that allows the S_L^{max} is found to be around 1.6, which corresponds to a Bilger mixture fraction $Z_{Bilger} = 0.045$ by using the definition shown below [55,56]:

$$Z_{Bilger} = \frac{(Z_H - Z_{H,os})/2M_H - (Z_O - Z_{O,os})/M_O}{(Z_{H,fs} - Z_{H,os})/2M_H - (Z_{O,fs} - Z_{O,os})/M_O} \quad (4)$$

where Z_H and Z_O are the mass fraction of H and O element, M_H and M_O are the relative atomic weight of H and O element, the subscripts 'fs' and 'os' represent the fuel stream and oxidizer stream, respectively. Fig. 3 shows the flame marker identified by the iso-contours of $Y_{H_2O} = 0.15$ and $Z_{Bilger} = 0.045$. It is clear that the flame marker is located at the leading edge of flame front with the high HRR and therefore is reliable to trace the hydrogen-air edge flame propagation in this study.

After identifying the position of flame marker, the flame displacement speed S_d at the flame marker can be evaluated using the following equation [12,57,58]:

$$S_d = \frac{1}{|\rho \nabla Y_P|}\left(\omega_P + \nabla \cdot (\rho D_P \nabla Y_P)\right) \quad (5)$$

where ρ is the density; Y_P is the product mass fraction; ω_P and D_P are the corresponding mass production rate and mass diffusion coefficient of product (here product is H_2O) in the multi-component mixture, respectively. The physical meaning of S_d is the propagation speed of iso-contour of product mass fraction relative to the local fluid, which is driven by the chemical production and mass diffusion of product species. To facilitate analyses on the influence of SD on the edge flame propagation, the S_d is further decomposed into three components ($S_d = S_{d,r} + S_{d,t} + S_{d,n}$) that correspond to the independent contribution of chemical reaction, tangential mass diffusion and normal mass diffusion, respectively [12,16]:

$$S_{d,r} = \frac{\omega_P}{\rho |\nabla Y_P|} \quad (6)$$

$$S_{d,t} = -D_P \cdot K \quad (7)$$

$$S_{d,n} = \frac{N_{Y_P} \cdot \nabla\left(\rho D_P N_{Y_P} \cdot \nabla Y_P\right)}{\rho |\nabla Y_P|} \quad (8)$$

where N_{Y_P} and K are the unit normal vector and local curvature of Y_P iso-contour and could be calculated as follows:

$$N_{Y_P} = -\frac{\nabla Y_P}{|\nabla Y_P|} \quad (9)$$

$$K = \nabla \cdot N_{Y_P} \quad (10)$$

Although the flame displacement speed S_d could describe the propagation speed of iso-contour of flame scalar relative to local fluid, it would be influenced by the thermal expansion and can be improper to indicate the flame propagation relative to unburnt mixture. Therefore, the density-weighted flame displacement speed $\tilde{S}_d$ is also adopted here to exclude the impacts of density change across the flame front:

$$\tilde{S}_d = \frac{\rho S_d}{\rho_u} \quad (11)$$

Since the hydrogen-air edge flame fronts studied here are naturally curved due to the strong transverse reactant concentration gradient, the responses of S_d and $\tilde{S}_d$ to flame curvature K, flame stretch rate

Table 1

The laminar flame speed S_L and flame thickness δ_f of hydrogen-air laminar premixed planar flame. (From PREMIX calculations [54], $\phi = 1.6$ and $Z_{Bilger} = 0.045$)

Case	S_L (cm/s)	δ_f (mm)
Soret	287.79	0.3437
noSoret	313.97	0.3520

κ and scalar dissipation rate χ under the effects of SD are also studied. The formula for calculating stretch rate κ could be expressed as follows [50]:

$$\kappa = \nabla \cdot \left[N_{Y_P} \times \left(U \times N_{Y_P} \right) \right] + \left(V_f \cdot N_{Y_P} \right) \left(\nabla \cdot N_{Y_P} \right) \tag{12}$$

where U is the local fluid speed and V_f is the propagation velocity of iso-contour of product mass fraction in the inertial coordinate system and given by $V_f = U + S_d \cdot N_{Y_P}$. Thus, the κ can be further expressed as follows [59]:

$$\kappa = \underbrace{\nabla \cdot \left[N_{Y_P} \times \left(U \times N_{Y_P} \right) \right]}_{\kappa_{st}} + \underbrace{\left(U \cdot N_{Y_P} \right) \cdot K}_{\kappa_{sn}} + \underbrace{S_d \cdot K}_{\kappa_c} \tag{13}$$

where the first term describes flame stretch induced by the tangential velocity gradient, namely flow strain term along the tangential direction therefore denoted as κ_{st}. Similarly, the second term is flow strain term along the normal direction and therefore denoted as κ_{sn}. The third term is flame stretch essentially induced by the flame curvature and denoted as κ_c.

The scalar dissipation rate χ can be calculated as follows:

$$\chi = 2D_Z \left| \nabla Z_{Bilger} \right|^2 \tag{14}$$

where D_Z is the global diffusivity of Bilger mixture fraction. Since the D_Z cannot be explicitly defined in our cases that consider the detailed mass diffusion process of multi-component mixture, here the local thermal diffusivity of mixture $\lambda/(\rho c_p)$ is used to retrieve the order of magnitude approximation of D_Z [30,60].

In addition, the normalizations of above parameters can be expressed as follows:

$$S_d^* = \frac{\tilde{S}_d}{S_L} = \frac{\rho S_d}{\rho_u S_L} \tag{15}$$

$$K^* = \frac{K}{1/\delta_f} \tag{16}$$

$$\kappa^* = \frac{\kappa}{S_L/\delta_f} = Ka \tag{17}$$

$$\chi^* = \frac{\chi}{S_L/\delta_f} = Da^{-1} \tag{18}$$

where the superscript $*$ denotes the normalization of corresponding parameters. ρ is the local density at the flame marker, ρ_u, S_L and δ_f are the unburnt gas density, fundamental laminar flame speed and flame thickness of the planar flame ($\phi = 1.6$ and $Z_{Bilger} = 0.045$). The δ_f can be assessed through $\delta_f = (T_b - T_u)/(\nabla T)_{max}$, where T_b and T_u are the burnt and unburnt temperature, $(\nabla T)_{max}$ is the maximum temperature gradient of a laminar premixed planar flame. The normalizations of κ and χ are also the Karlovitz number (Ka) and inverse of Damköhler number (Da^{-1}) that provide the magnitude scaling of chemical time to flow time and chemical time to diffusion time, respectively. The S_L and δ_f of hydrogen-air laminar premixed planar flames with and without SD are listed in Table 1.

3. Results and discussions

Surrounding goals that investigating the impacts of SD on the hydrogen-air edge flame dynamics and the diffusion-chemistry interaction, we first present the macroscopic views on the evolution of

propagating hydrogen-air edge flames in the following sub-sections. Then the responses of flame displacement speed to flame curvature, stretch rate and scalar dissipation rate in two cases are analyzed. After indicating the non-negligible influences of SD on the edge flame dynamics, we finally study the difference of flame structure as a result of the diffusion-chemistry interaction.

3.1. Ignition and evolution of edge flame

Fig. 4 shows the evolution of contours of HRR, H and H_2 mass fraction between $t = 0.02$ and 1.2 ms in the Soret case. It can be seen that a flame kernel with the obvious heat release is developed at 0.02 ms while the tri-brachial flame structure is not formed yet. Meanwhile, the flame kernel grows initially towards the lean side due to the exact location of stoichiometric line within the mixing layer. The flame index defined as $\xi = \nabla Y_{H_2} \cdot \nabla Y_{O_2}$ [61] is also computed here to differentiate various flame branches. Such definition of ξ indicates the inner product of fuel and oxidizer concentration gradients. Then the positive flame index suggests the rich and lean premixed flame branches (RPFB and LPFB in Fig. 4) and the negative one corresponds to the diffusion flame branch (DFB in Fig. 4). Thus, the iso-contour of $\xi = 0$ in Fig. 4 (white dashed line) shall be considered as the boundary between different flame branches. At $t = 0.02$ ms, a region bounded by the iso-contour of $\xi = 0$ is primarily on the rich side and the high HRR region at the initial stage is mostly in the DFB. After the successful ignition, a tri-brachial flame structure begins to emerge at around 0.4 ms. The premixed zone identified by the iso-contour of $\xi = 0$ extends towards the lean side and forms the LPFB. By referencing together with the HRR contours, the DFB is found to share a strong heat release zone with the RPFB and LPFB, suggesting that the DFB would supply energy for the development of LPFB during the formation of tri-brachial flame structure. In addition, the comparison between contours of H and H_2 reveals that H is more abundant on the burnt side, while H_2 is mainly concentrated on the upstream (right side) of $Y_{H_2O} = 0.15$ iso-contour and thus close to the unburnt side, which suggests different distribution features of H and H_2 in the edge flame structure.

Figs. 5a and 5b depict the evolutions of flame position and HRR at the flame marker in two cases. It is clear in Fig. 5a that the instantaneous position of edge flame in the noSoret case is always ahead of that in the Soret case, suggesting that SD mildly suppresses the edge flame propagation. Such effects are similar to those on the hydrogen-air premixed flames. The HRR profiles in Fig. 5b both show an initially rapid descending stage (before $t = 0.1$ ms) followed by a relatively mild rising stage. When SD is considered, the initial chemical reaction ignited by a high temperature region in the spatially stratified layer is enhanced by the additional diffusion provided by SD, which could be reflected by the higher initial HRR profile. This is quite consistent with the observation from Fig. 4 (at $t = 0.02$ ms) where the high HRR region is located in the DFB. The enhancement effects of SD on such a diffusion-controlled process are similar to what were found in the non-premixed flames [44]. The descending HRR profile suggests that the flame temperature is transitioning to the self-sustainable value after the edge flame is ignited. During the propagation process, the curvature of edge flame front (cf. $Y_{H_2O} = 0.15$ iso-contour in Fig. 4) would decrease due to the transverse diffusion (along the y-direction) of upstream reactants and thus leads to the rising trend of HRR profiles. Moreover, the noSoret case shows a higher HRR profile during the later stage of flame propagation, which in turn results in the faster propagation shown in Fig. 5a. Such effects of SD on the edge flame propagation are more like those on premixed flames. Fig. 5c shows the correlation of flame displacement speed S_d with stretch rate κ during the whole flame propagation process within the computational domain. It could be seen that the S_d-κ correlation shows the linear feature (blue symbols) after the initial ignition and formation stage of triple flame (black symbols). Moreover, when the flame is approaching close to right boundary, the S_d-κ correlation is also influenced and the
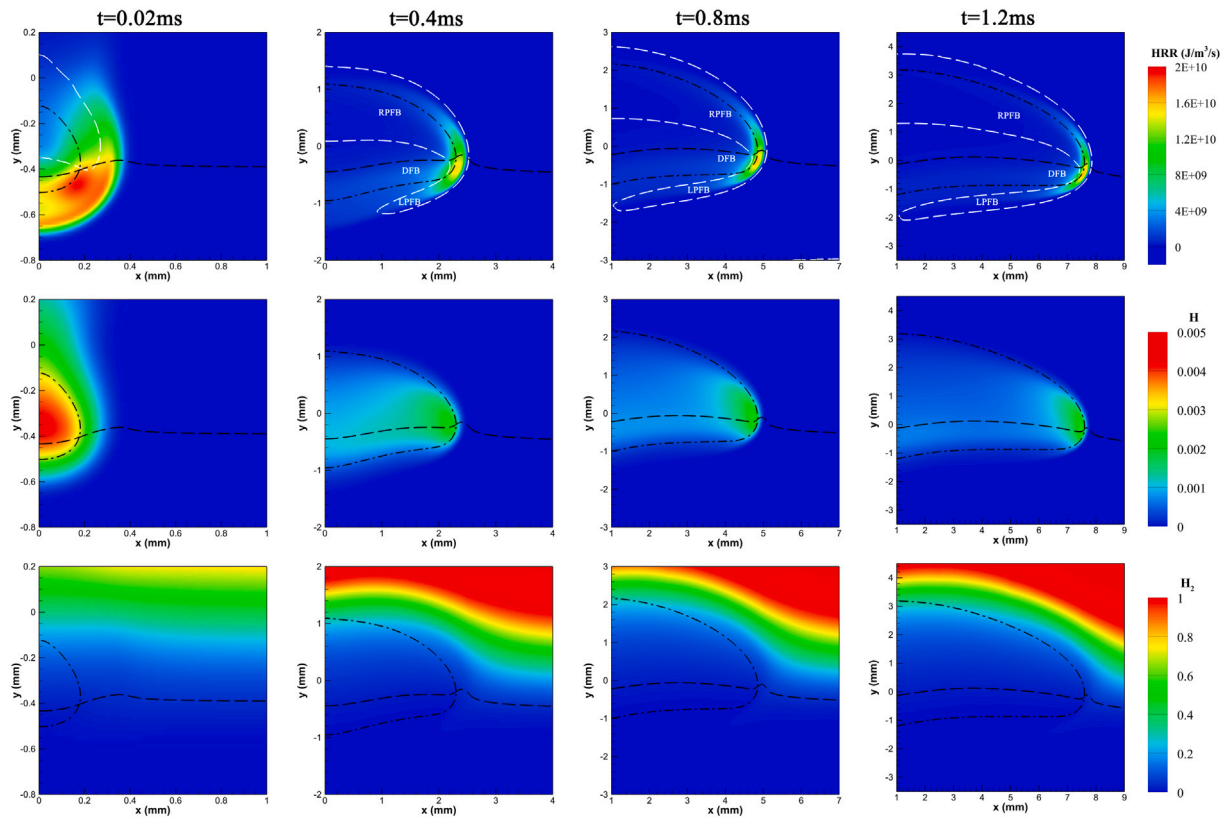
Fig. 4. The evolution of HRR, H and H_2 mass fraction during edge flame propagation. (The white dashed line is iso-contour of $\xi = 0$, the black dashed line and black dot-dashed line are iso-contours of $Z_{Bilger} = 0.045$ and $Y_{H_2O} = 0.15$.).
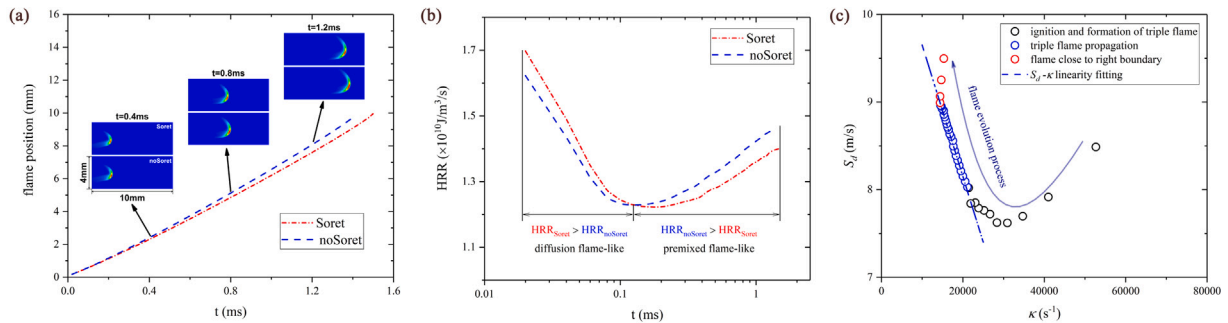

Fig. 5. (a) The evolution of flame position (x-coordinate of flame marker) with the temporal time. (b) The evolution of HRR at the flame marker with the temporal time. (c) The correlation of flame displacement speed S_d with stretch rate κ during the flame propagation process (Soret case, blue data are without initial and end boundary effects and hence are used for analyses in following subsections.). (For interpretation of the references to colour in this figure legend, the reader is referred to the web version of this article.)

linear relationship fails (red symbols). To avoid potential influence of domain size and ignition source on our results and analyses in following subsections, we only use the data points in linear regime (blue symbols) and other data points are discarded.

3.2. Soret effects on flame responses

As there exists the curvature variation during the edge flame propagation (cf. Fig. 4), the potential effects of curvature and stretch on the partially premixed flame dynamics [30,62,63] shall be considered. Although the edge flame dynamics has been analyzed in some previous studies [12,28,34], it is of importance to further investigate the effects of SD on the responses of flame displacement speed S_d to curvature K, stretch rate κ and scalar dissipation rate χ (i.e. Eqs. (5) to (18)).

Fig. 6a shows the responses of flame displacement speed S_d and its three components to flame curvature K. Note that during the flame

propagation, the flame curvature, stretch rate and scalar dissipation rate at the flame marker would decrease simultaneously due to that the transverse diffusion of upstream reactants alters the local mixture composition and decreases the reactant gradient before the flame front arrives. It is clear that the $S_{d,t}$-K correlations in two cases both exhibit the linear feature owing to the intrinsic linear curvature dependence of $S_{d,t}$ in Eq. (7). Under same curvature, the magnitudes of $S_{d,t}$ show small difference due to the close D_{H_2O} at flame marker in two cases. Moreover, the negative values of $S_{d,t}$ suggest its role in decreasing the S_d.

As also shown in Fig. 6a, the $S_{d,n}$ only vary within 0.05 m/s, which means that the $S_{d,n}$ is insensitive to the curvature and SD does not exert much influence on the $S_{d,n}$. It is worth noting that the local flame thickness or local product layer thickness δ_P ($\delta_P \sim 1/|\nabla Y_P|$ according to simple scaling) would be important for the $S_{d,n}$ due to its direct relevance with the normal diffusion process. Fig. 7a shows
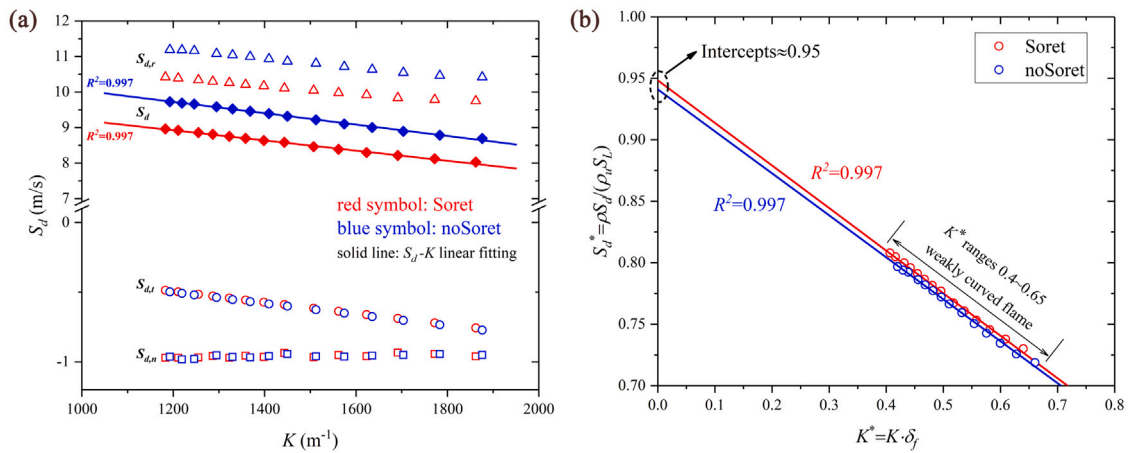
Fig. 6. (a) The response of flame displacement speed S_d and its three components to flame curvature K. (b) The responses of density-weighted normalized flame displacement speed S_d^* to normalized flame curvature K^*.
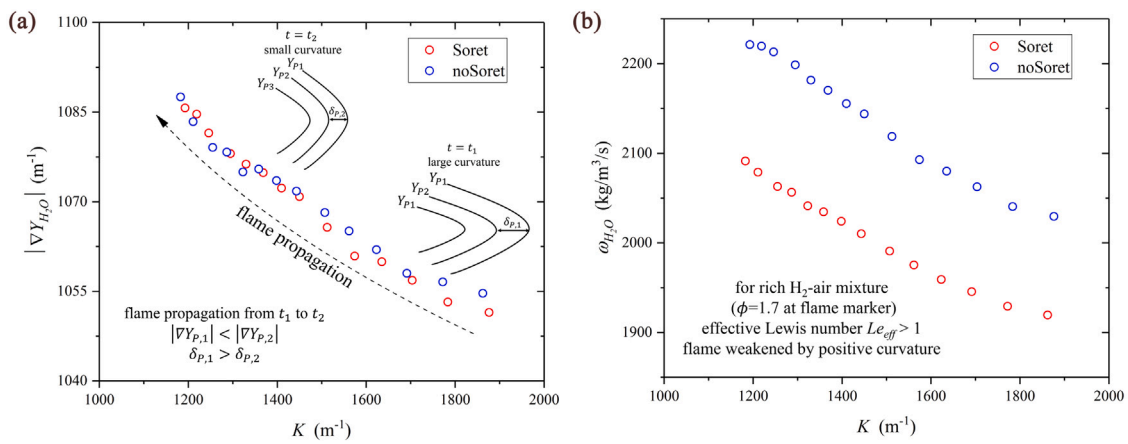

Fig. 7. The response of (a) product mass fraction gradient $\left|\nabla Y_{H_2O}\right|$ and (b) product mass production rate ω_{H_2O} to flame curvature K.
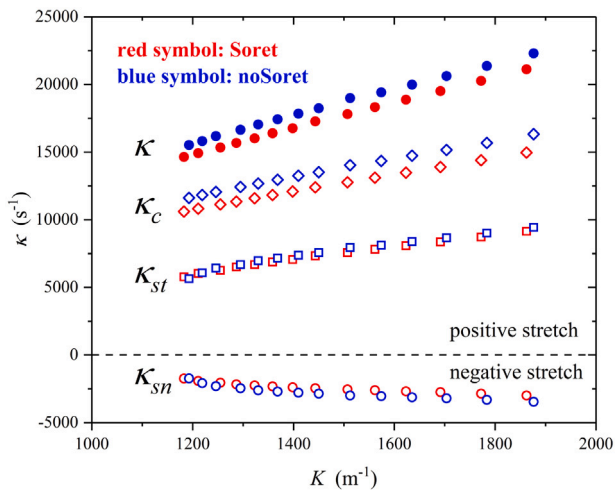

Fig. 8. The dependence of flame stretch rate on flame curvature at the flame marker.

the profiles of $\left|\nabla Y_{H_2O}\right|$ under different curvatures. The overall trend suggests that as the edge flame propagates, the reduction of flame front curvature is accompanied with the increase of $\left|\nabla Y_{H_2O}\right|$. Such increase of $\left|\nabla Y_{H_2O}\right|$ should be due to the thinning of product layer thickness (from $\delta_{P,1}$ to $\delta_{P,2}$ as illustrated in the inset of Fig. 7a) as a result of

decreasing curvature. The connection between δ_P and K seems to be mostly geometrical so that the difference of $\left|\nabla Y_{H_2O}\right|$ between two cases is quite small. The subtle contribution of $\left|\nabla Y_{H_2O}\right|$ (i.e. $\left|\nabla Y_P\right|$ in Eq. (8)) to the $S_{d,n}$ variation should be attributed to the explicit appearance of $\left|\nabla Y_P\right|$ in both numerator and denominator of Eq. (8). In Table 1 (cf. Section 2.4), the flame thickness of uncurved planar flame δ_f almost does not affected by SD, which could be considered as the special case of δ_P (as $K \to 0$) that is shown to be almost independent of SD in Fig. 7a.

Since it is found in Fig. 6a that the chemical reaction term $S_{d,r}$ shall dominate the S_d behavior because $\left|S_{d,r}\right| \gg \left|S_{d,n}\right| > \left|S_{d,t}\right|$, and the $S_{d,r}$ in the noSoret case is significantly larger under same curvature, Fig. 7b shows the product mass production rate ω_{H_2O} as a preliminary assessment of the importance of chemical reactions. As shown, the Soret case exhibits a noticeably smaller production rate compared with the noSoret case. This suggests that because SD is diffusion-related, the mass diffusion of small and reactive molecules into or away from the reaction zone is the substantial reason that the flame displacement speed is decreased due to SD.

For hydrogen-air mixture at the flame marker where the equivalence ratio is 1.6, the corresponding effective Lewis number Le_{eff} is revealed to be about 1.5 according to research results of Sun [64], Bechtold [65] and Joulin [66]. Therefore, the negative ω_{H_2O}-K correlations in Fig. 7b are principally induced by the inequality between heat and mass diffusion for the curved flame front when the effective Lewis number is larger than 1. It is worth noting that some previous studies [12,28] used the one-step chemical reaction model and the
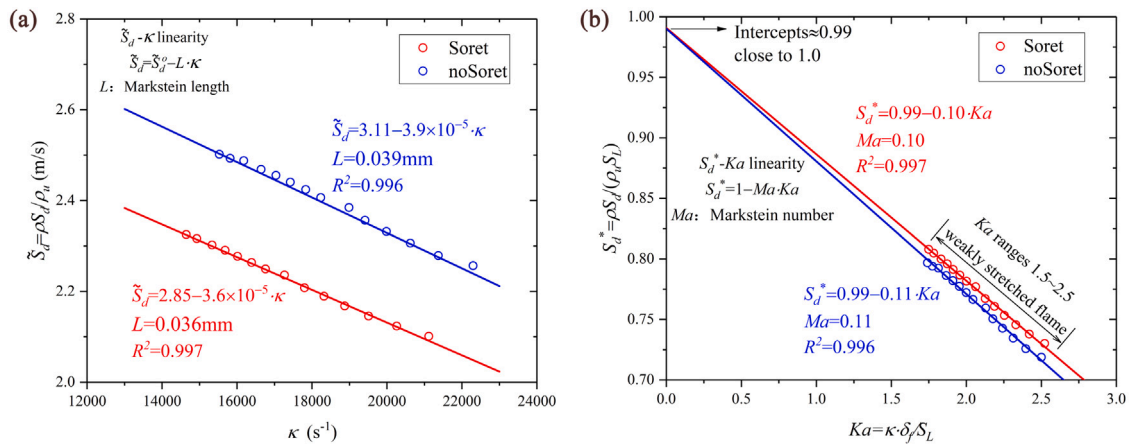
Fig. 9. (a) The response of density-weighted flame displacement speed $\tilde{S}_d$ to flame stretch rate κ. (b) The response of density-weighted normalized flame displacement speed S_d^* to Karlovitz number Ka. (For interpretation of the references to colour in this figure legend, the reader is referred to the web version of this article.)
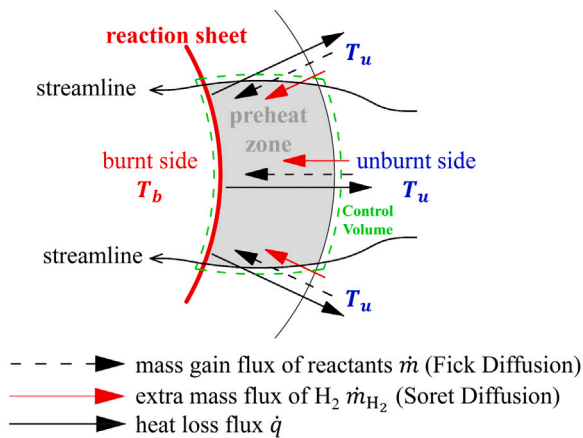

Fig. 10. The schematic of the smaller Markstein length of edge flame with Soret diffusion.

unity Lewis number assumption. Hence the product mass production rate was shown to be almost independent of flame curvature. The $S_{d,r}(= \omega_P/(\rho|\nabla Y_P|))$ was then positively correlated with flame curvature K in these studies, which should be mainly caused by the negative $|\nabla Y_P|$-K correlation similar to Fig. 7a. When the multi-component transport is taken into consideration, the thermo-chemical state of mixture at the flame marker would vary, and the ω_{H_2O} shows an obvious negative dependence on flame curvature. Such inconsistency in analyzing the $S_{d,r}$-K relationship between this study and previous investigations implies that it is important to consider the detailed transport process of multi-component mixture in such a problem.

In addition, Fig. 6a demonstrates the overall response of flame displacement speed S_d to flame curvature K, in which the negative linear S_d-K correlation are observed in two cases. Based on above analyses, it can be concluded that the negative S_d-K correlation should result from the combination of $S_{d,t}$ and $S_{d,r}$ profiles. The slopes of S_d-K correlations in two cases in Fig. 6a are revealed to differ weakly with each other. This means that the sensitivity of S_d to flame curvature K could largely be the geometrical curvature effects and SD plays a role partly. Fig. 6b shows how the normalized flame displacement speed S_d^* varies with the normalized curvature K^*. Since K^* is smaller than 0.65, the edge flames studied here could be considered to be weakly curved, which could account for the linear dependence of S_d on K, and S_d^* on K^*.

Due to the curved flame front of edge flame, the re-direction effect [15] and simultaneous flame stretch caused by flow strain and

flame curvature would also emerge. The flame stretch has been proven to have remarkable impacts on the edge flame propagation [30,34] and thus is also analyzed here. Fig. 8 shows the total stretch κ and its three terms κ_{st}, κ_{sn}, and κ_c (cf. Eq. (13)) under different curvatures. The normal component of flow strain term κ_{sn} is the only negative term among three components, which is due to the local fluid velocity U being opposite to the N_{Y_P}, yielding a negative inner product $U \cdot N_{Y_P}$. The tangential component of flow strain term κ_{st} is positive and its absolute values are larger than those of κ_{sn}. Compared with the weak influence of SD on profiles of κ_{sn} and κ_{st}, SD causes a relatively appreciable difference of κ_c profiles between two cases. Since $\kappa_c = S_d \cdot K$ by definition, the κ_c is larger in the noSoret case because of the larger S_d under same curvature. Since the S_d also decreases with increasing curvature K, the κ_c-K correlation is not rigorously linear. The total flame stretch rate κ increases with increasing curvature K and the obvious difference between two cases seems to primarily stem from κ_c. It is also revealed that SD, interacting with chemical reactions, directly affects the S_d and associated flame stretch.

Fig. 9 shows the response of $\tilde{S}_d$ to κ, and S_d^* to Ka. It is clear that the $\tilde{S}_d$-κ and S_d^*-Ka correlations are quite linear in two cases, which is qualitatively consistent with the flame stretch theory [50] that has been commonly used in the premixed flame scenario. Note that such theory can still be extended to analyze the dynamics of edge flame (partially premixed flame) [34]. Applying the flame stretch theory to our edge flame problems, $S_d^* = 1 - Ma \cdot Ka$ where Ma is the Markstein number of edge flame here and is anticipated to be equal to the slope of S_d^*-Ka linearity in Fig. 9b. Similarly, the slope of $\tilde{S}_d$-κ plot can be treated as the Markstein length (L) of edge flame. As shown in Fig. 9, the case considering SD shows the smaller L and Ma.

Fig. 10 is a summary schematic of mass and heat diffusion flux in the proximity of flame front to account for the smaller Markstein length L and Markstein number Ma of edge flame when including SD. The fact that $Le_{eff} = 1.5 > 1$ means that the mass gain $\dot{m}$ would be not as strong as the heat loss $\dot{q}$ in Fig. 10. If one considers a control volume (like the green dotted line in Fig. 10) for a curved edge flame (with a positive stretch), the imbalance between mass and heat fluxes across the lateral surfaces, i.e. the top and bottom of control volume, shall essentially weaken the edge flame. Because the effective Lewis number considers both Fick mass diffusion and thermal energy diffusion, the relatively stronger thermal energy diffusion would induce a greater heat loss and therefore the $\tilde{S}_d$ of a stretched edge flame is reduced. This is the reason accounting for the positive L and Ma shown in Fig. 9. When SD is considered, there would be an extra flux of hydrogen $\dot{m}_{H_2}$ driven by SD from the unburnt side (low temperature) to the reaction sheet (high temperature). This flux $\dot{m}_{H_2}$ is partly "compensating" the reduction of $\tilde{S}_d$ with increasing stretch rate, and thus the L and Ma are
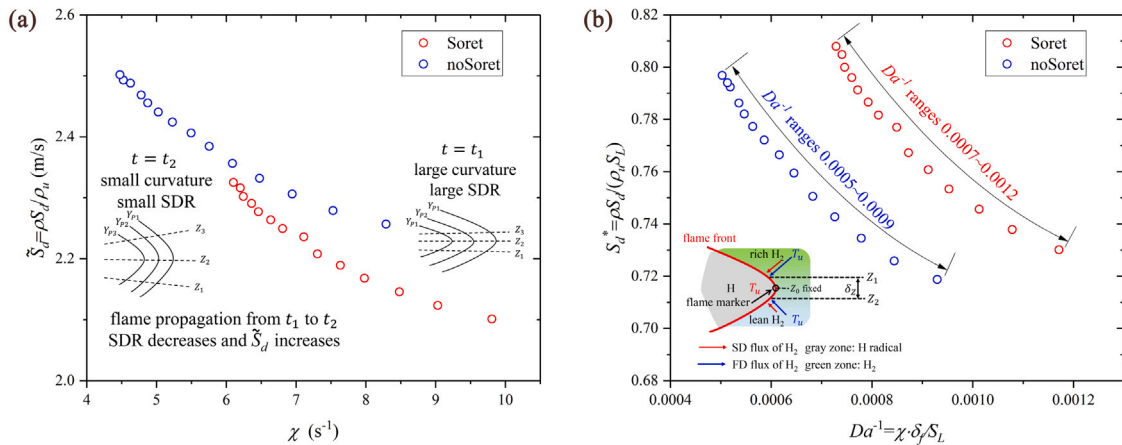
Fig. 11. (a) The response of density-weighted flame displacement speed $\tilde{S}_d$ to scalar dissipation rate χ. (b) The response of density-weighted normalized flame displacement speed S_d^* to inverse of Damköhler number Da^{-1}. (For interpretation of the references to colour in this figure legend, the reader is referred to the web version of this article.)
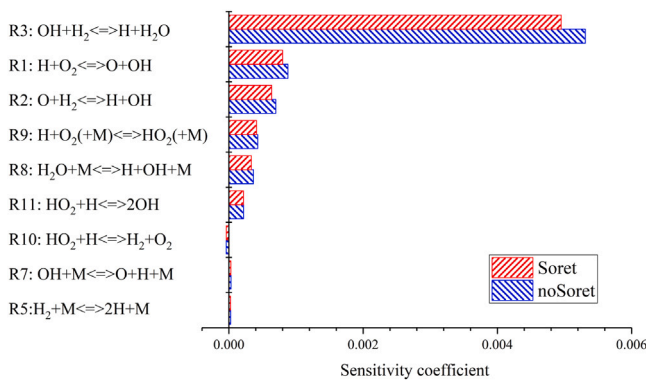

Fig. 12. The results of sensitivity analysis of H_2O mass fraction to individual chemical reaction. (The local composition at the flame marker in two cases at 0.8 ms are used here.)

smaller in the Soret case. Similar impacts of SD on L and Ma were also found in the theoretical analysis about the two-reactant flames [37] and the numerical simulation of syngas-air outwardly propagating spherical flames [67].

If one extrapolates the S_d^*-Ka linearity shown in Fig. 9b, it will intercept with $Ka = 0$ (unstretched condition) at $S_d^* = 0.99$ in two cases. Thus, in the positive stretch region, these two intercepts indicate that the $\tilde{S}_d$ would still be bounded by the laminar flame speed S_L, and therefore is consistent with Dold's theory [14] about the edge flame dynamics.

The scalar dissipation rate can also exert noticeable influences on the edge flame dynamics [28,30]. Since SD could affect the mass transfer process and the mass fraction distribution of individual species, especially H and H_2, it can be envisioned that SD would influence the response of density-weighted flame displacement speed $\tilde{S}_d$ to scalar dissipation rate χ. Fig. 11 shows the response of $\tilde{S}_d$ to χ, and S_d^* to Da^{-1}. Note that the scalar dissipation rate would be decreasing during flame propagation due to the transverse diffusion along the y-direction. It is also clear in Fig. 7b that the mass production rate of product H_2O ω_{H_2O} becomes higher simultaneously, which reveals the negative correlation of reaction intensity with scalar dissipation rate. As the scalar dissipation rate means the timescale of local scalar mixing, a smaller χ is indicative of a longer mixing process and hence more complete chemical reaction. This is also the reason for the negative $\tilde{S}_d - \chi$ and $S_d^* - Da^{-1}$ correlations shown in Fig. 11. In addition, unlike the linear $\tilde{S}_d$-K and $\tilde{S}_d$-κ correlations, the negative dependence of $\tilde{S}_d$ on χ is found to be non-linear obviously, which is consistent

with previous studies [17,28]. Fig. 11b shows distinctly different S_d^*-Da^{-1} profiles, in which the profile of the Soret case seems to shift towards the larger Da^{-1} regime. The inset of Fig. 11b shows the potential contributions of FD and SD fluxes of H_2 in two cases. After FD establishes the basic fluxes pointing to the flame front (blue arrows in Fig. 11b), SD would affect the H element transport through the SD flux of H_2 (red arrows in Fig. 11b) and increase the local mixture fraction (Z_1 and Z_2 in Fig. 11b). The augment of Z_1 would be larger due to the higher H_2 concentration and the larger SD flux at the fuel rich side (cf. Figs. 14d and 15d). Based on $\chi = D_Z \left(\frac{Z_1 - Z_2}{\delta_Z} \right)^2$, the scalar dissipation rate χ would also be increased, which indicates the effects of SD on changing the local scalar mixing. The different ranges of χ and Da^{-1} also suggest that it may be necessary to include SD when modeling the hydrogen-air edge flame based the flamelet generation manifold, in which the mixture fraction and the scalar dissipation rate are often used to construct the flamelet library [60,68].

3.3. Reaction sensitivity and diffusion flux analysis

From the discussion in Section 3.2, it could be seen that SD has non-negligible effects on the edge flame dynamics. The impacts of SD are found to be mainly reflected by the chemical reaction component of flame displacement speed. Thus, this section inherits such trend of thought and would discuss the diffusion-chemistry interaction, i.e. chemical reactions, local composition, and mass diffusion process in two cases.

The important reactions for edge flame propagation in this study are identified through sensitivity analysis. The sensitivity coefficient of H_2O mass fraction to individual reaction is calculated here due to its relevance with the determination of flame marker. The sensitivity coefficient here indicates the first order partial derivative of species mass fraction with respect to reaction rate coefficients by varying the pre-exponential "A-factors" in the Arrhenius reaction-rate expressions [69]. Fig. 12 shows the results of sensitivity analysis based on local composition at the flame market at 0.8 ms (cf. Fig. 5b, in the premixed flame-like stage). Although the sensitivity coefficients vary slightly between two cases, the important reactions are identical due to the similar local composition and temperature at the flame marker. As shown in Fig. 12, $OH+H_2 \Leftrightarrow H+H_2O$ (R3), $H+O_2 \Leftrightarrow O+OH$ (R1); $O+H_2 \Leftrightarrow H+OH$ (R2); $H+O_2(+M) \Leftrightarrow HO_2(+M)$ (R9) are four important reactions for the H_2O production. These reactions are also usually regarded as main chemical pathways related with reactions of H and H_2 in the hydrogen-air system, and would be further analyzed.

The curvature dependence of reaction rates of above four reactions is depicted in Fig. 13a, in which reaction rates are all weakened in the Soret case. R3 is the main chemical pathway of H_2O production, and
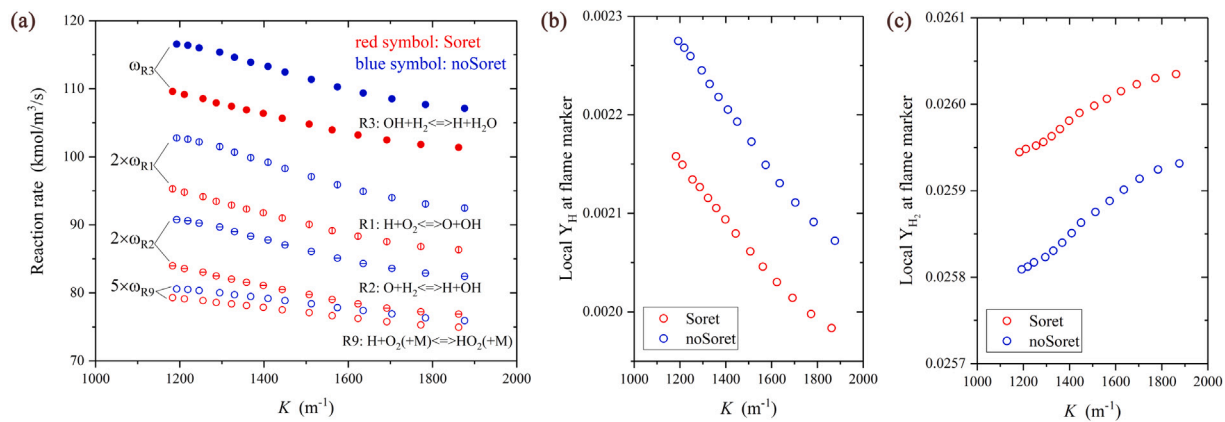
Fig. 13. The curvature dependence of (a) reaction rates of important chemical reactions and local mass fraction of (b) H and (c) H_2 at the flame marker.

the absolute difference of it caused by SD is obviously larger than that of other reactions. The trend of ω_{R3}-K profile is also quite consistent with the ω_{H_2O}-K curve in Fig. 7b. Moreover, these reaction rates tend to decrease with increasing curvature K, but the difference between Soret and noSoret cases seems to remain the same under different curvatures, suggesting that SD plays more important roles than flame curvature in the difference of reaction rates.

To further understand the effects of SD on the edge flame structure, the local mass fraction of H and H_2 at the flame marker are depicted in Figs. 13b and 13c, respectively. It is found that local mass fraction profiles of H_2 and H show the completely opposite dependence on flame curvature, which means that the geometrical effects of increasing curvature intrinsically alter the flame structure. In addition, SD has noticeably different effects on the mass fractions of H_2 (as the fuel and driven into the reaction zone by SD) and H (as an intermediate and driven away from the reaction zone by SD). The mass fraction of H_2 is found to be around 0.026 and increased by SD about 0.4%, whereas that of H is about 0.0022 and reduced by SD about 4.8%, i.e. obviously stronger than the change of H_2 mass fraction.

It is worth noting that SD would cause obvious difference of reaction component of flame displacement speed $S_{d,r}$ rather than two diffusion components $S_{d,n}$ and $S_{d,t}$ in Fig. 6a. This means that the chemical reaction would be influenced by SD because of the change of local composition. For different concentrations of reactants (especially H and H_2), the reaction rate would be different even the flame dynamics parameters show similar effects on flame speed S_d and $\tilde{S}_d$ in two cases. The flame speeds differ with each other even the curvatures, stretch rates and scalar dissipation rates are same in two cases (cf. Figs. 6, 9 and 11), which demonstrates that the change of local composition and reaction rate due to SD is a fundamental reason for larger S_d and $\tilde{S}_d$ in noSoret case. Being one special case, the planar premixed flame whose curvature, stretch rate and scalar dissipation rate are all equal to zero, the laminar flame speed S_L is also revealed to be larger when SD is not considered (cf. Table 1).

Considering the flame marker in Fig. 3 tracing the flame front with strong chemical reaction, the weaker effects of SD on the mass fraction of H_2 than that of H in Figs. 13b and 13c might imply weaker impacts of SD on the H_2 diffusion flux. To clearly illustrate this characteristics, the distributions of HRR, components of driving force of SD, i.e. $\nabla T/T$ or $\nabla (lnT)$, and mass fluxes of H_2 and H arising from FD and SD along the normal direction of flame front in the two-dimensional Z_{Bilger}-Y_{H_2O} space are shown in Fig. 14. Fig. 14a first shows the distribution of HRR, in which the obvious exothermic region is located within the narrow Z_{Bilger} band ranging 0.02~0.05 and the wide Y_{H_2O} band ranging 0.02~0.2. The intersection of two dashed lines is the location of flame marker in the Z_{Bilger}-Y_{H_2O} space, and it is clear that the flame marker is located in the high HRR region. Fig. 14b shows that although the $[\nabla (lnT)]_N$ is coupled with the HRR along the Z_{Bilger} coordinate, it is

more concentrated on the low Y_{H_2O} side, which suggests that the driving force of SD is stronger on the unburnt side near the flame marker due to the low temperature (hence the high $\nabla T/T$). It is quite evident in Fig. 14c that the variation of $j_{H_2}^{(FD)_N}$ is highly related with the Z_{Bilger}, indicating that the $j_{H_2}^{(FD)_N}$ mostly prevails on the fuel rich side where the $j_{H_2}^{(FD)_N}$ shows a negative value and large magnitude, and it is still considerably strong near the flame marker. Fig. 14d shows the normal component of SD flux of H_2, in which the $j_{H_2}^{(SD)_N}$ shall be primarily affected by the driving force strength presented in Fig. 14b as well as the absolute concentration of species. Compared with the $j_{H_2}^{(FD)_N}$, the high $j_{H_2}^{(SD)_N}$ zone is concentrated within the Z_{Bilger} band ranging 0.02~0.1, indicating that the $j_{H_2}^{(SD)_N}$ is strongly coupled with the large $[\nabla (lnT)]_N$ region along the Z_{Bilger} coordinate. With the contribution of absolute concentration of H_2, the $j_{H_2}^{(SD)_N}$ also seems to be more inclined towards the fuel-rich side (or the preheat zone, rather than the reaction zone) due to the demand on fuel supply. The $j_{H_2}^{(SD)_N}$ at the flame marker is therefore relatively weak, which is consistent with the weak effects of SD on the H_2 mass fraction shown in Fig. 13c. Figs. 14e and 14f show the normal components of FD and SD fluxes of H, respectively. They are found to distribute in a way similar to the HRR near the flame marker but show opposite signs (positive $j_H^{(FD)_N}$ and negative $j_H^{(SD)_N}$). In addition, the $j_H^{(SD)_N}$ is mainly located surrounding the flame marker, or the Y_{H_2O} band ranging 0.1~0.2, which clearly demonstrates that the $j_H^{(SD)_N}$ is occurring near the center of reaction zone, on the burnt side, rather than the preheat zone because of the distribution feature of H in the edge flame structure.

Fig. 15 shows the tangential and normal components of different diffusion flux terms of H_2 and H to conduct the further quantitative comparison. Practically, the extraction of these flux components is based on the location of Y_{H_2O} = 0.15 iso-contour. The tangential component shown in Figs. 15a and 15b are at the order of 10^{-3} kg/m^2/s, obviously weaker than the normal components (at the order of 10^{-2} kg/m^2/s) shown in Figs. 15c and 15d, which indicates that the normal fluxes of H_2 and H contribute much more in species diffusion than the tangential flux. This inherent feature is inevitable due to the large gradients of mass fraction and temperature as the driving force of FD and SD. The $j_{H_2}^{(FD)_N}$ and the $j_{H_2}^{(SD)_N}$ in Fig. 15c are both negative, while the $j_H^{(FD)_N}$ and the $j_H^{(SD)_N}$ in Fig. 15d are with opposite signs. Note that the normal direction of flame front points into the unburnt side according to $\mathbf{N}_{Y_P} = -\nabla Y_P/|\nabla Y_P|$ in Fig. 15e. Because SD would transport H_2 and H from low to high temperature region, namely from the unburnt side to the burnt side of edge flame, the $j_{H_2}^{(SD)_N}$ and the $j_H^{(SD)_N}$ are both negative. Compared with the positive $j_H^{(FD)_N}$ that is driven by the concentration gradient from the reaction zone towards the preheat zone, the negative $j_H^{(SD)_N}$ means that the SD flux of H generates a 'counter' mass flux induced by the temperature gradient.
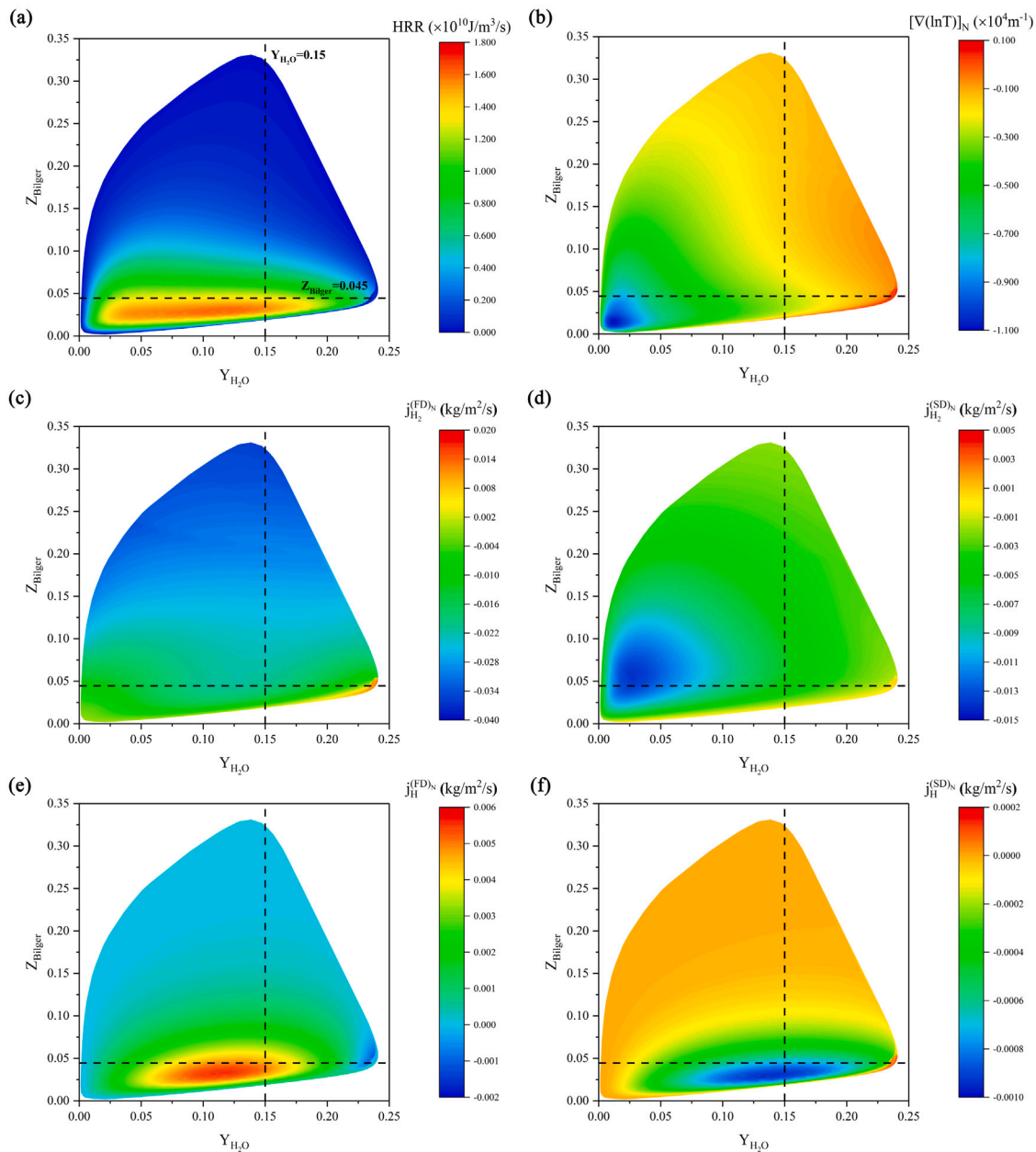
Fig. 14. The distribution of (a) HRR, normal component of (b) $\nabla(lnT)$, (c) FD flux of H_2, (d) SD flux of H_2, (e) FD flux of H and (f) SD flux of H in the Z_{Bilger}-Y_{H_2O} space. (The normal components of FD and SD fluxes of H and H_2 could be calculated through (take H as an example) $j_H^{(FD)_N} = \boldsymbol{j}_H^{FD} \cdot \boldsymbol{N}_{Y_P} = \left(\rho Y_H \left(\boldsymbol{U}_H^F + \boldsymbol{U}^{C,F}\right)\right) \cdot \boldsymbol{N}_{Y_P}$ and $j_H^{(SD)_N} = \boldsymbol{j}_H^{SD} \cdot \boldsymbol{N}_{Y_P} = \left(\rho Y_H \left(\boldsymbol{U}_H^S + \boldsymbol{U}^{C,S}\right)\right) \cdot \boldsymbol{N}_{Y_P}$, respectively (cf. Eqs. (3) and (9)). The normal component of $\nabla(lnT)$ could also be calculated as $[\nabla(lnT)]_N = \nabla(lnT) \cdot \boldsymbol{N}_{Y_P}$. The data of the Soret case at 0.8 ms is used here.)

When SD is considered, the mass diffusion flux of H along the normal direction would be suppressed while that of H_2 would be enhanced, which is clearly revealed by $\left|j_{H_2}^{(FD+SD)_N}\right| > \left|j_{H_2}^{(FD)_N}\right|$ and $\left|j_H^{(FD+SD)_N}\right| < \left|j_H^{(FD)_N}\right|$ in Figs. 15c and 15d. This process caused by SD would reduce the local H mass fraction (cf. Fig. 13b) and should be the fundamental reason that the chemical reaction component of flame displacement speed $S_{d,r}$ is decreased due to SD (cf. Fig. 6a). Besides, it is clear in Figs. 15c and 15d that the difference of $j_H^{(FD)_N}$ profiles between the Soret and noSoret case is most pronounced around the flame marker, while the $j_{H_2}^{(FD)_N}$ profiles differs with each other at the fuel rich side when the Z_{Bilger} is obviously larger than 0.045. This is a direct evidence for the stronger effects of SD on the transport of H than that of H_2 at the flame marker.

Fig. 16 summarizes the analyses on H and H_2 diffusion in the edge flame. Due to the fact that H forms on the burnt side and H_2 is more

on the unburnt side, the FD fluxes of H and H_2 are both towards the flame front through the $\boldsymbol{j}_{H_2}^{FD}$ and the $\boldsymbol{j}_H^{FD}$ with opposite directions (blue arrows in Fig. 16). As the temperature gradient always points from the unburnt side to the burnt side, the $\boldsymbol{j}_{H_2}^{SD}$ and the $\boldsymbol{j}_H^{SD}$ (red arrows in Fig. 16) are consequently in same direction. Therefore, the total diffusion flux of H $\boldsymbol{j}_H^{FD+SD}$ (left black arrow) would be smaller than the $\boldsymbol{j}_H^{FD}$ (left blue arrow). On the contrary, the total flux of H_2 $\boldsymbol{j}_{H_2}^{FD+SD}$ (right black arrow) is larger than the $\boldsymbol{j}_{H_2}^{FD}$ (right blue arrow) because of synergistic effects of the FD and SD fluxes of H_2. This difference demonstrates the opposite effects of SD on the mass transport of H and H_2 in the hydrogen-air edge flame. Moreover, for the curved edge flame front, the enhanced flux of H_2 arising from SD through the lateral surface of flame front control volume and the simultaneous diffusion-chemistry interaction are also the fundamental reasons for the smaller sensitivity of displacement speed to flame stretch.
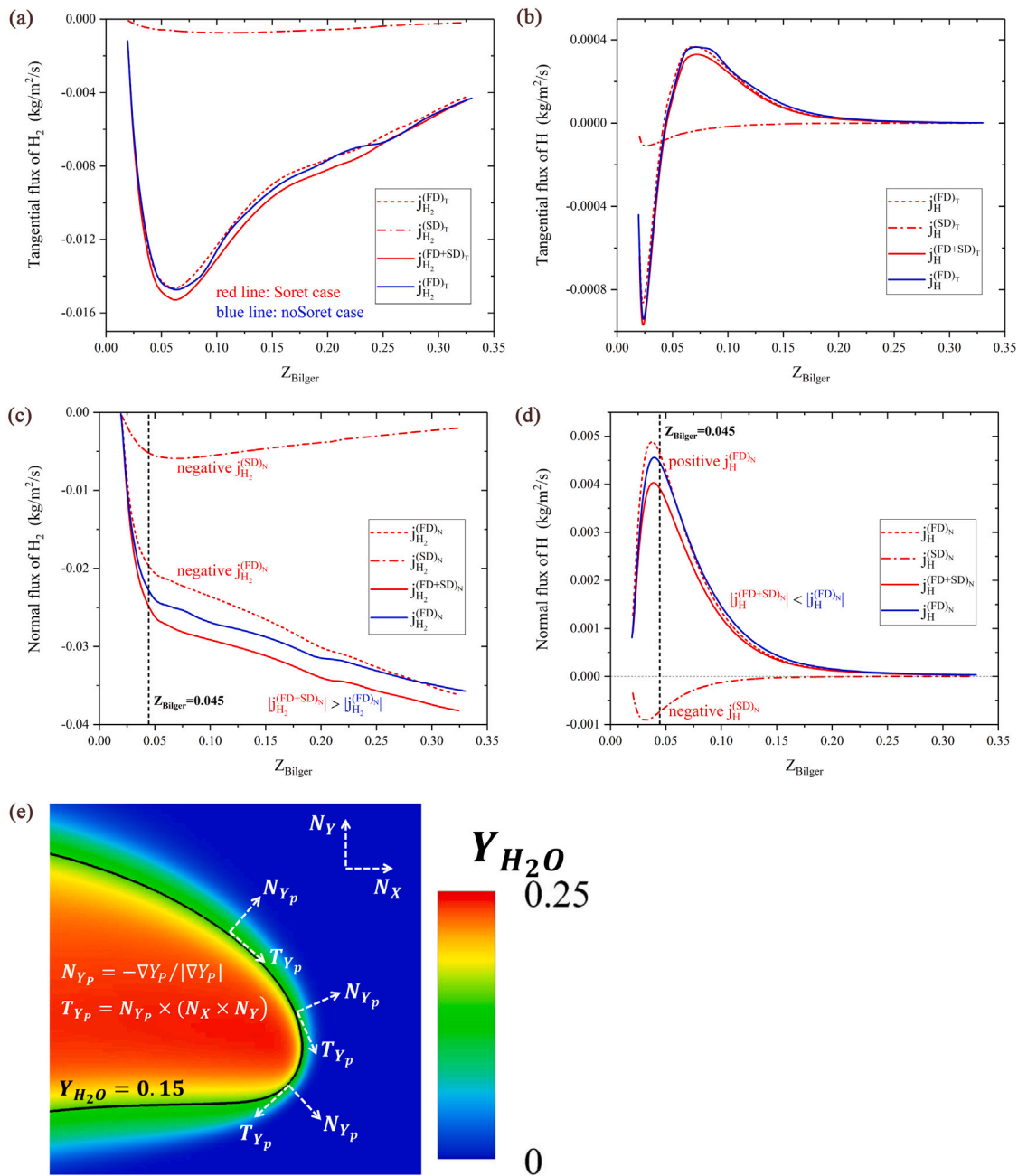
Fig. 15. The comparison of tangential component of (a) H_2 and (b) H diffusion flux, normal component of (c) H_2 and (d) H diffusion flux. (e) The schematic of tangential and normal unit vector of flame front. (As shown by Fig. 15e, the unit normal vector is given as $N_{Y_p} = -\nabla Y_P/|\nabla Y_P|$, then the unit tangential vector is determined through the vector cross product as $T_{Y_p} = N_{Y_p} \times (N_X \times N_Y)$ where N_X and N_Y are the unit vectors along the x-coordinate and the y-coordinate respectively. Take the j_H^{FD} as an example, its normal and tangential component could be calculated as $j_H^{(FD)_N} = j_H^{FD} \cdot N_{Y_p}$ and $j_H^{(FD)_T} = j_H^{FD} \cdot T_{Y_p}$. Moreover, the flux caused by the SD is zero in the noSoret case and therefore $j_H^{FD+SD} = j_H^{FD}$, and only the j_H^{FD} profile is depicted as the blue solid line. The data of two cases at 0.8 ms are used here.). (For interpretation of the references to color in this figure legend, the reader is referred to the web version of this article.)

4. Conclusions

The effects of Soret diffusion (SD) on the diffusion-chemistry interaction of hydrogen-air edge flames propagating in transverse gradient evolving mixing layers are numerically investigated in this study. The freely-propagating edge flames within hydrogen-air mixing layers with SD (Soret case) and without SD (noSoret case) are simulated by the numerical code *MultiDiffFOAM*. After identifying the flame marker, the responses of flame displacement speed S_d and its tangential diffusion component $S_{d,t}$, normal diffusion component $S_{d,n}$ and chemical reaction component $S_{d,r}$, to flame curvature K, and responses of density-weighted flame displacement speed $\tilde{S}_d$ to flame stretch rate κ and scalar

dissipation rate χ are analyzed. The sensitivity analysis is utilized to find out important chemical reactions with further analyses on local reaction rates and species mass fraction. The diffusion fluxes of H_2 and H are shown in the two-dimensional Z_{Bilger}-Y_{H_2O} space with discussion about the diffusion-chemistry interaction near the flame marker. The key conclusions from the above efforts are summarized as follows:

• During the initial ignition stage, the edge flames develop from a flame kernel into a tri-brachial structure. The heat release rate (HRR) in the diffusion flame branch is shown to be weaker compared with that in the premixed flame branch. During the propagation process, the edge flame without considering SD shows a faster propagation and the
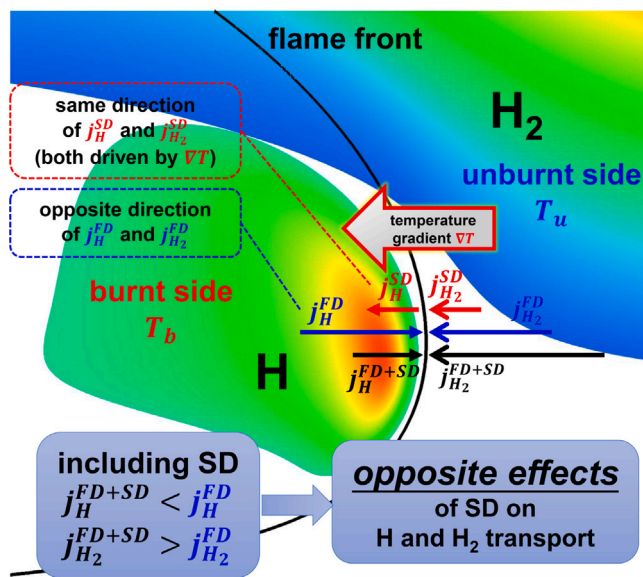
Fig. 16. The schematic of Soret effects on the diffusion-chemistry interaction: the opposite impacts of Soret diffusion on H and H_2 transport in the edge flame structure.

HRR at the flame marker also consistently shows a higher profile in the noSoret case.

• For the negative linear $S_{d,t}$-K correlation, the values of $S_{d,t}$ in two cases show weak difference because of the close local mass diffusivity of product (represented by D_{H_2O}). Moreover, SD shows weak effects on the $S_{d,n}$ profiles due to the close product mass fraction gradient under same curvature. However, excluding SD would lead to the considerably larger $S_{d,r}$, which is resulted from the SD effects on mass production rate of product. Both the S_d-K and $\tilde{S}_d$-κ correlations are negative and linear because the edge flames in this study are weakly curved and stretched, while the $\tilde{S}_d$-χ correlation is revealed to be negative nonlinear. The extrapolation of $\tilde{S}_d$ to the unstretched condition based on the fitting of S_d^*-Ka data in two cases both reveals that the $\tilde{S}_d$ would be bounded by the laminar flame speed S_L. Moreover, SD is found to cause the smaller Markstein length and Markstein number because of the lateral "compensating" flux of H_2 into the flame front.

• The important reactions are revealed to be OH+H_2⇔H+H_2O (R3), H+O_2⇔O+OH (R1); O+H_2⇔H+OH (R2); H+O_2(+M)⇔HO_2(+M) (R9) based on the sensitivity analysis and the rates of these reactions are all obviously smaller in the Soret case. Meanwhile, SD shows opposite effects on the local mass fraction of H_2 and H at the flame marker. The SD flux of H_2 $j_{H_2}^{SD}$ and H j_H^{SD} are both strongly coupled with the driving force $\nabla(lnT)$ along the Z_{Bilger} coordinate. Moreover, the $j_{H_2}^{SD}$ is promoted on the unburnt side while the j_H^{SD} is situated on the burnt side, which is due to the different distribution features of H and H_2 in edge flame structure. When considering SD, the normal components of H_2 flux caused by FD $j_{H_2}^{(FD)_N}$ and by SD $j_{H_2}^{(SD)_N}$ are in the same direction and the total H_2 flux $j_{H_2}^{(FD+SD)_N}$ is strengthened. While for H, the $j_H^{(FD)_N}$ and the $j_H^{(SD)_N}$ are in the opposite directions. Thus, SD would create a 'counter' diffusion flux of H that could weaken the local reactivity and lead to a smaller $S_{d,r}$, which is the main reason for the slower propagation of edge flame in the Soret case.

CRediT authorship contribution statement

Tao Chen: Conceptualization, Methodology, Software, Validation, Formal analysis, Investigation, Data curation, Writing – original draft. **Suyuan Yu:** Writing – review and editing, Project administration, Funding acquisition. **Yu Cheng Liu:** Writing – review & editing, Visualization, Project administration, Funding acquisition, Resources.

Declaration of competing interest

The authors declare that they have no known competing financial interests or personal relationships that could have appeared to influence the work reported in this paper.

References

[1] Han W, Dai P, Gou X, Chen Z. A review of laminar flame speeds of hydrogen and syngas measured from propagating spherical flames. Appl Energy Combust Sci 2020;1–4:100008. http://dx.doi.org/10.1016/j.jaecs.2020.100008.

[2] Fayaz H, Saidur R, Razali N, Anuar F, Saleman A, Islam M. An overview of hydrogen as a vehicle fuel. Renew Sustain Energy Rev 2012;16(8):5511–28. http://dx.doi.org/10.1016/j.rser.2012.06.012.

[3] Chintala V, Subramanian K. A comprehensive review on utilization of hydrogen in a compression ignition engine under dual fuel mode. Renew Sustain Energy Rev 2017;70:472–91. http://dx.doi.org/10.1016/j.rser.2016.11.247.

[4] Seyam S, Dincer I, Agelin-Chaab M. Novel hybrid aircraft propulsion systems using hydrogen, methane, methanol, ethanol and dimethyl ether as alternative fuels. Energy Convers Manage 2021;238:114172. http://dx.doi.org/10.1016/j.enconman.2021.114172.

[5] Bazooyar B, Shariati A, Khosravi-Nikou M, Hashemabadi SH. Numerical analysis of nitrogen oxides in turbulent lifted H2/N2 cabra jet flame issuing into a vitiated coflow. Int J Hydrogen Energy 2019;44(26):13932–52. http://dx.doi.org/10.1016/j.ijhydene.2019.03.166.

[6] Oh J, Yoon Y. Flame stabilization in a lifted non-premixed turbulent hydrogen jet with coaxial air. Int J Hydrogen Energy 2010;35(19):10569–79. http://dx.doi.org/10.1016/j.ijhydene.2010.07.146.

[7] Babayev R, Andersson A, Dalmau AS, Im HG, Johansson B. Computational characterization of hydrogen direct injection and nonpremixed combustion in a compression-ignition engine. Int J Hydrogen Energy 2021;46(35):18678–96. http://dx.doi.org/10.1016/j.ijhydene.2021.02.223.

[8] Kahraman N, Tangöz S, Akansu SO. Numerical analysis of a gas turbine combustor fueled by hydrogen in comparison with jet-A fuel. Fuel 2018;217:66–77. http://dx.doi.org/10.1016/j.fuel.2017.12.071.

[9] Wu C-Y, Chen K-H. Characterization of hydrogen triple flame propagation in vitiated laminar coaxial flow. Int J Hydrogen Energy 2014;39(26):14109–19. http://dx.doi.org/10.1016/j.ijhydene.2014.06.155.

[10] Quattrocchi S, Aggarwal SK, Katta VR. Liftoff and blowout characteristics of laminar syngas nonpremixed flames. Int J Hydrogen Energy 2018;43(12):6421–33. http://dx.doi.org/10.1016/j.ijhydene.2018.01.194.

[11] Buckmaster J. Edge-flames. Prog Energy Combust Sci 2002;28(5):435–75. http://dx.doi.org/10.1016/S0360-1285(02)00008-4.

[12] Karami S, Hawkes ER, Talei M, Chen JH. Edge flame structure in a turbulent lifted flame: A direct numerical simulation study. Combust Flame 2016;169:110–28. http://dx.doi.org/10.1016/j.combustflame.2016.03.006.

[13] Phillips H. Flame in a buoyant methane layer. Symp (Int) Combust 1965;10(1):1277–83. http://dx.doi.org/10.1016/S0082-0784(65)80262-4.

[14] Dold J. Flame propagation in a nonuniform mixture: analysis of a slowly varying triple flame. Combust Flame 1989;76(1):71–88. http://dx.doi.org/10.1016/0010-2180(89)90079-5.

[15] Ruetsch G, Vervisch L, Liñán Martínez A. Effects of heat release on triple flames. Phys Fluids 1995;7(6):1447–54. http://dx.doi.org/10.1063/1.868531.

[16] Chen T, Yu S, Liu YC. Effects of pressure on propagation characteristics of methane-air edge flames within two-dimensional mixing layers: A numerical study. Fuel 2021;301:120857. http://dx.doi.org/10.1016/j.fuel.2021.120857.

[17] Ghosal S, Vervisch L. Theoretical and numerical study of a symmetrical triple flame using the parabolic flame path approximation. J Fluid Mech 2000;415:227–60. http://dx.doi.org/10.1017/S0022112000008685.

[18] Ko Y, Chung SH. Propagation of unsteady tribrachial flames in laminar non-premixed jets. Combust Flame 1999;118(1–2):151–63. http://dx.doi.org/10.1016/S0010-2180(98)00154-0.

[19] Chung SH. Stabilization, propagation and instability of tribrachial triple flames. Proc Combust Inst 2007;31(1):877–92. http://dx.doi.org/10.1016/j.proci.2006.08.117.

[20] Mulla IA, Chakravarthy SR. Propagation velocity and flame stretch measurements in co-flowing partially premixed flames with widely varying premixedness. Combust Flame 2013;160(8):1345–56. http://dx.doi.org/10.1016/j.combustflame.2013.02.001.

[21] Buckmaster J, Zhang Y. Oscillating edge-flames. Combust Theory Model 1999;3(3):547. http://dx.doi.org/10.1088/1364-7830/3/3/307.

[22] Watson K, Lyons K, Donbar J, Carter C. Scalar and velocity field measurements in a lifted CH4–air diffusion flame. Combust Flame 1999;117(1–2):257–71. http://dx.doi.org/10.1016/S0010-2180(98)00086-8.

[23] Watson K, Lyons K, Donbar J, Carter C. On scalar dissipation and partially premixed flame propagation. Combust Sci Technol 2003;175(4):649–64. http://dx.doi.org/10.1080/00102200302393.

[24] Lyons K, Watson K, Carter C, Donbar J. Upstream islands of flame in lifted-jet partially premixed combustion. Combust Sci Technol 2007;179(5):1029–37. http://dx.doi.org/10.1080/00102200600910858.

[25] Lyons KM. Toward an understanding of the stabilization mechanisms of lifted turbulent jet flames: experiments. Prog Energy Combust Sci 2007;33(2):211–31. http://dx.doi.org/10.1016/j.pecs.2006.11.001.

[26] Buckmaster J, Weber R. Edge-flame-holding. Symp (Int) Combust 1996;26(1):1143–9. http://dx.doi.org/10.1016/S0082-0784(96)80330-4.

[27] Karami S, Hawkes ER, Talei M, Chen JH. Mechanisms of flame stabilisation at low lifted height in a turbulent lifted slot-jet flame. J Fluid Mech 2015;777:633–89. http://dx.doi.org/10.1017/jfm.2015.334.

[28] Chakraborty N, Mastorakos E. Numerical investigation of edge flame propagation characteristics in turbulent mixing layers. Phys Fluids 2006;18(10):105103. http://dx.doi.org/10.1063/1.2357972.

[29] Im HG, Chen JH. Structure and propagation of triple flames in partially premixed hydrogen–air mixtures. Combust Flame 1999;119(4):436–54. http://dx.doi.org/10.1016/S0010-2180(99)00073-5.

[30] Im HG, Chen JH. Effects of flow strain on triple flame propagation. Combust Flame 2001;126(1–2):1384–92. http://dx.doi.org/10.1016/S0010-2180(01)00261-9.

[31] Owston R, Abraham J. Numerical study of hydrogen triple flame response to mixture stratification, ambient temperature, pressure, and water vapor concentration. Int J Hydrogen Energy 2010;35(10):4723–35. http://dx.doi.org/10.1016/j.ijhydene.2010.02.049.

[32] Owston R, Abraham J. Flame propagation in stratified hydrogen–air mixtures: Spark placement effects. Int J Hydrogen Energy 2009;34(15):6532–44. http://dx.doi.org/10.1016/j.ijhydene.2009.05.089.

[33] Owston R, Magi V, Abraham J. Some numerical considerations in the simulation of low-Ma number hydrogen/air mixing layers. Int J Hydrogen Energy 2010;35(23):12936–44. http://dx.doi.org/10.1016/j.ijhydene.2010.08.139.

[34] Briones AM, Aggarwal SK, Katta VR. Effects of H2 enrichment on the propagation characteristics of CH4–air triple flames. Combust Flame 2008;153(3):367–83. http://dx.doi.org/10.1016/j.combustflame.2008.02.005.

[35] Giovangigli V. Multicomponent transport in laminar flames. Proc Combust Inst 2015;35(1):625–37. http://dx.doi.org/10.1016/j.proci.2014.08.011.

[36] Han W, Scholtissek A, Dietzsch F, Hasse C. Effects of soret diffusion on turbulent non-premixed H2 jet flames. Combust Flame 2020;213:39–51. http://dx.doi.org/10.1016/j.combustflame.2019.11.029.

[37] García-Ybarra P, Nicoli C, Clavin P. Soret and dilution effects on premixed flames. Combust Sci Technol 1984;42(1–2):87–109. http://dx.doi.org/10.1080/00102208408960370.

[38] Ern A, Giovangigli V. Thermal diffusion effects in hydrogen-air and methane-air flames. Combust Theory Model 1998;2(4):349. http://dx.doi.org/10.1088/1364-7830/2/4/001.

[39] Dixon-Lewis G. Kinetic mechanism, structure and properties of premixed flames in hydrogen—oxygen—nitrogen mixtures. Phil. Trans. R. Soc. A 1979;292(1388):45–99. http://dx.doi.org/10.1098/rsta.1979.0045.

[40] Faghih M, Han W, Chen Z. Effects of soret diffusion on premixed flame propagation under engine-relevant conditions. Combust Flame 2018;194:175–9. http://dx.doi.org/10.1016/j.combustflame.2018.04.031.

[41] Grcar JF, Bell JB, Day MS. The soret effect in naturally propagating, premixed, lean, hydrogen–air flames. Proc Combust Inst 2009;32(1):1173–80. http://dx.doi.org/10.1016/j.proci.2008.06.075.

[42] Sánchez AL, Williams FA. Recent advances in understanding of flammability characteristics of hydrogen. Prog Energy Combust Sci 2014;41:1–55. http://dx.doi.org/10.1016/j.pecs.2013.10.002.

[43] Yang F, Law CK, Sung C, Zhang H. A mechanistic study of soret diffusion in hydrogen–air flames. Combust Flame 2010;157(1):192–200. http://dx.doi.org/10.1016/j.combustflame.2009.09.018.

[44] Arias-Zugasti M, Rosner DE. Soret transport, unequal diffusivity, and dilution effects on laminar diffusion flame temperatures and positions. Combust Flame 2008;153(1–2):33–44. http://dx.doi.org/10.1016/j.combustflame.2007.12.005.

[45] Dietzsch F, Scholtissek A, Hunger F, Hasse C. The impact of thermal diffusion on the structure of non-premixed flames. Combust Flame 2018;194:352–62. http://dx.doi.org/10.1016/j.combustflame.2018.05.018.

[46] Briones A, Puri IK, Aggarwal SK. Effect of pressure on counterflow H2–air partially premixed flames. Combust Flame 2005;140(1–2):46–59. http://dx.doi.org/10.1016/j.combustflame.2004.10.003.

[47] Hilbert R, Tap F, El-Rabii H, Thévenin D. Impact of detailed chemistry and transport models on turbulent combustion simulations. Prog Energy Combust Sci 2004;30(1):61–117. http://dx.doi.org/10.1016/j.pecs.2003.10.001.

[48] Kee RJ, Warnatz J, Miller JA. Fortran computer-code package for the evaluation of gas-phase viscosities, conductivities, and diffusion coefficients. Livermore, CA (USA): Sandia National Labs.; 1983.

[49] Chen T, Liu YC. Effects of gravity level on morphology of laminar double flames. In: ASME 2019 international mechanical engineering congress and exposition, American Society of Mechanical Engineers Digital Collection https://doi.org/10.1115/IMECE2019-11051.

[50] Law CK. Combustion physics. Cambridge University Press; 2010.

[51] Viggiano A, Magi V. A 2-D investigation of n-heptane autoignition by means of direct numerical simulation. Combust Flame 2004;137(4):432–43. http://dx.doi.org/10.1016/j.combustflame.2004.03.003.

[52] Ó Conaire M, Curran HJ, Simmie JM, Pitz WJ, Westbrook CK. A comprehensive modeling study of hydrogen oxidation. Int J Chem Kinet 2004;36(11):603–22. http://dx.doi.org/10.1002/kin.20036.

[53] Issa RI. Solution of the implicitly discretised fluid flow equations by operator-splitting. J Comput Phys 1986;62(1):40–65. http://dx.doi.org/10.1016/0021-9991(86)90099-9.

[54] Kee RJ, Grcar JF, Smooke MD, Miller JA, Meeks E. PREMIX: a Fortran program for modeling steady laminar one-dimensional premixed flames. Sandia national laboratories report, SAND85-8249, 1985.

[55] Bilger R, Stårner S, Kee R. On reduced mechanisms for methane-air combustion in nonpremixed flames. Combust Flame 1990;80(2):135–49. http://dx.doi.org/10.1016/0010-2180(90)90122-8.

[56] Sutherland J, Smith P, Chen J. Quantification of differential diffusion in nonpremixed systems. Combust Theory Model 2005;9(2):365–83. http://dx.doi.org/10.1080/17455030500150009.

[57] Pope S. The evolution of surfaces in turbulence. Internat J Engrg Sci 1988;26(5):445–69. http://dx.doi.org/10.1016/0020-7225(88)90004-3.

[58] Echekki T, Chen JH. Structure and propagation of methanol–air triple flames. Combust Flame 1998;114(1–2):231–45. http://dx.doi.org/10.1016/S0010-2180(97)00287-3.

[59] Qin X, Choi CW, Mukhopadhyay A, Puri IK, Aggarwal SK, Katta VR. Triple flame propagation and stabilization in a laminar axisymmetric jet. Combust Theory Model 2004;8(2):293. http://dx.doi.org/10.1088/1364-7830/8/2/006.

[60] Owston R, Abraham J. Exploratory studies of modeling approaches for hydrogen triple flames. Int J Hydrogen Energy 2011;36(14):8570–82. http://dx.doi.org/10.1016/j.ijhydene.2011.03.048.

[61] Yamashita H, Shimada M, Takeno T. A numerical study on flame stability at the transition point of jet diffusion flames. Symp (Int) Combust 1996;26(1):27–34. http://dx.doi.org/10.1016/S0082-0784(96)80196-2.

[62] Chakraborty N, Cant S. Unsteady effects of strain rate and curvature on turbulent premixed flames in an inflow–outflow configuration. Combust Flame 2004;137(1–2):129–47. http://dx.doi.org/10.1016/j.combustflame.2004.01.007.

[63] Hawkes ER, Chen JH. Evaluation of models for flame stretch due to curvature in the thin reaction zones regime. Proc Combust Inst 2005;30(1):647–55. http://dx.doi.org/10.1016/j.proci.2004.08.106.

[64] Sun C, Sung C-J, He L, Law CK. Dynamics of weakly stretched flames: quantitative description and extraction of global flame parameters. Combust Flame 1999;118(1–2):108–28. http://dx.doi.org/10.1016/S0010-2180(98)00137-0.

[65] Bechtold J, Matalon M. The dependence of the markstein length on stoichiometry. Combust Flame 2001;127(1–2):1906–13. http://dx.doi.org/10.1016/S0010-2180(01)00297-8.

[66] Joulin G, Mitani T. Linear stability analysis of two-reactant flames. Combust Flame 1981;40:235–46. http://dx.doi.org/10.1016/0010-2180(81)90127-9.

[67] Liang W, Chen Z, Yang F, Zhang H. Effects of soret diffusion on the laminar flame speed and Markstein length of syngas/air mixtures. Proc Combust Inst 2013;34(1):695–702. http://dx.doi.org/10.1016/j.proci.2012.06.048.

[68] Van Oijen J, De Goey L. A numerical study of confined triple flames using a flamelet-generated manifold. Combust Theory Model 2004;8(1):141. http://dx.doi.org/10.1088/1364-7830/8/1/008.

[69] Kee R, Rupley F, Miller J, Coltrin M, Grcar J, Meeks E, et al. CHEMKIN theory manual. USA: Reaction Design; 2006.